Parameter optimization of GTN model parameters for SLM process

by
Arnab Majumdar

Mini-Thesis

Faculty of Mechanical Engineering
RWTH Aachen University

This thesis was supervised by:
Research assistant: MSc. Heyuan Wang
Responsible professor: Univ.-Prof. Dr.-Ing C. Broeckmann
Institute for Materials Applications in Mechanical Engineering (IWM), RWTH Aachen

Aachen, September 2018

Table of Contents

1 Abstract

Gurson-Tvergaard-Needleman (GTN) model is very famous as a plastic damage model for parts with voids. The parts produced by Selective Laser Melting (SLM) process have more voids compared to those produced by conventional methods. Therefore GTN model can be used for describing the failure of a SLM processed part. However, GTN model introduces unknown parameters which can not be measured by experiments. Therefore, we are trying to obtain these parameters through data analysis in this work. During this work, data taken from the stress-strain curve as an input and the unknown parameters are predicted by linear regression on input data. The Stress-strain curve are generated using ABAQUS for different combination of parameter values. Thereafter, these are divided into training set of data and test set of data. Training set of data is used to determine the regression function and then the determined function applied on the test set of data for prediction of unknown parameters. The predicted data is then compared with the original data. Last but not least, the Bayesian approach is introduced to analyse the data base and its results tell us how to supplement the data base to yield better results.

2 Introduction

2.1 Selective Laser Melting

Additive manufacturing is gaining its popularity day by day in the manufacturing industry due to its efficiency in creating complex geometries. During 1980s, additive manufacturing emerged as a new technology for manufacturing parts. However, during its initial days it could only be used for producing prototypes to accelerate the development process. Due to a lack of reliability, parts produced by additive manufacturing could not be used directly in the applications. In recent times, with the advancement of technology the manufacturing sector has coped up with a lot of the challenges associated with additive manufacturing. Currently additive manufacturing is being used for manufacturing metal-based parts like stainless steel [1, 2, 3], Ti-6Al-4V [4, 5] and nickel based alloys [6] for direct use. The fuel nozzle for the LEAP engine of GE Aviation [7, 8], Lockheed's blead detector [9], biomedical cranial and hip implants [10, 11, 12] are live examples of parts produced by additive manufacturing for direct use. Due to these successes, additive manufacturing has generated a lot of interest amongst researchers, industry and even public media [13, 14, 15].

Although additive manufacturing has overcome a lot of obstacles, there are still a lot left. To use additive manufacturing as a mainstream manufacturing technology, obstacles like part quality, reproducibility, lack of materials and process standards must be addressed. A lot of researchers and industrial stakeholders are trying to find a way to overcome these challenges. Modelling and simulation can provide a lot of insight to the designers and testers in understanding the behaviour of additive manufacturing parts. Apart from that, real world testing can be expensive sometimes. Therefore, it is not at all feasible to conduct a test for every design change made in the process of product development. Simulation results can give the designers an approximate result before the testing. Also, in the case of additive manufacturing, there are a lot of process parameters and complex physical transformations, which can make the process difficult to understand through controlled experiments. During simulation, these controlled experiments can be done very easily.

In this work, selective Laser melting (SLM) is considered for further investigation. SLM is one type of additive manufacturing process. This technique uses high power-density laser to fuse the metal powder. SLM was introduced in 1995 by Fraunfoher Institute for Laser Technology in Aachen. Now a days it has found a copious amount of applications in the field of manufacturing, especially in light weight designing. This happened because in the field of Aerospace a lot of complex surfaces are required to be made. Traditional manufacturing methods are not cost-effective solution to these requirements.

In figure 1 a schematic diagram of SLM process has been presented. In the left side of the figure, a schematic diagram of set-up is made. As can be seen, during SLM a metal powder bed is created and a constant feed to this bed is provided. The laser beam melts the powder

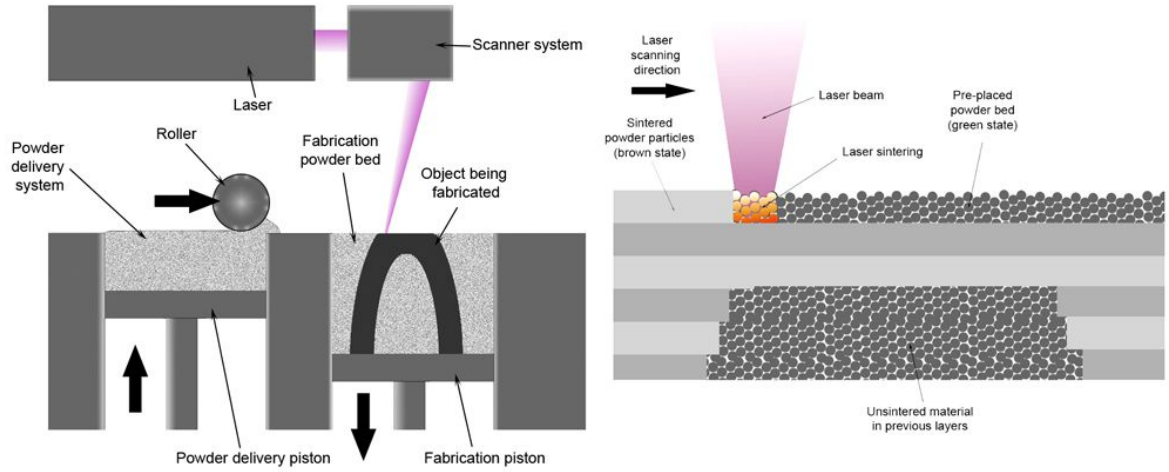

Figure 1 Left side: Schematic diagram of SLM set-up, Right side: Schematic diagram of SLM process, see [16]

layer by layer to create the final product. In the right side, a schematic diagram of the melting process is presented.

As can be understood from the nature of process that there will be process induced voids in the parts produced through this method. A lot of works are being done to make the void fraction lesser by controlling the process parameter, see [17] for an example. However, there are very few studies about the damage mechanism of the SLM products. In this work a ductile damage constitutive model is implemented in parts produced by SLM.

2.2 GTN model

For modelling the damage of the parts produced by SLM process Gurson-Tvergaard-Needleman (GTN) model is implemented in this work. GTN model is a well known damage model for modelling the yield surface, which considers the voids at the micro level. This model got its initial shape through the work of Gurson in 1977. He proposed a model for growth of void in an ideal plastic material, see [18]. Later Tvergaard and Needleman did further modifications to this model, see [19]. In honour of their work, this model is named after them and is known as GTN model. Although it is very useful to use this model for describing the plastic behaviour because of its inclusion of the micro-mechanical effect of the material, this model has a significant disadvantage. This model need 12 parameters and all of them can not be measured directly by experimental method. Usually this parameters are obtained by comparing the load displacement curve of simulation and experiment. Lot of parameter optimization methods are proposed in order to find these parameters for different applications. In [20] a gradiant based method is proposed to minimize the least square functional to predict the force-necking of stE690 steel during tensile test. In [20] an approximated inverse function is generated from the load dis-

placement curve to predict the material parameters in a Small Punch Test (SPT).

The GTN model is a widely used model for modelling of ductile fractures. This model includes the micro-mechanical effect in the description of yield surface. This model also exhibits hydrostatic stress dependence in strain softening due to presence of voids in micro level. This particular phenomenon separates this model from the classical plasticity. Ductile damage in metals can be classified into following phases: void nucleation, void growth, strain localisation and necking between voids, coalescence and fracture. In figure 2, all these phases of ductile

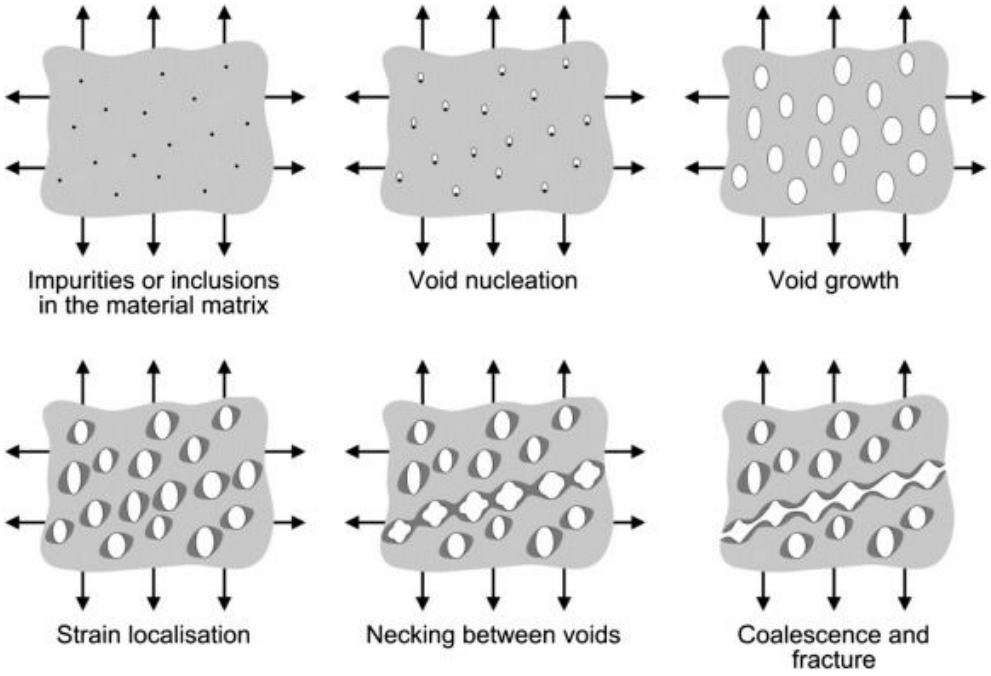

Figure 2 Different phases of ductile fracture, see [21] for reference

fracture are shown.

To include the micro mechanical effect of voids the isotropic Von-Mises yield potential is modified as following.

$$\begin{aligned} \Phi &= \left(\frac{\sigma_v}{\sigma_y}\right)^2 + 2q_1 f^* \cosh\left(\frac{3}{2} q_2 \frac{\sigma_m}{\sigma_y}\right) - (1 + q_3 f^*) \\ &= 0 \\ \text{With } \sigma_v &= \sqrt{\frac{3}{2} \cdot S_{ij} \cdot S_{ij}} \text{ and } \sigma_m = \frac{1}{3} \cdot \sigma_{kk} \end{aligned} \tag{2.1}$$

where Φ is the yield potential, σ_v is the Von-Mises equivalent stress, S_{ij} is Cauchy stress, σ_y is the yield or flow stress of the material and σ_m is the hydrostatic stress. In this case, the damage variable is the volume fraction of voids or the porosity, termed as f^*. In [22] Tvergaard introduced the model parameters q_1, q_2 and q_3 in order to fit the model results with the experimental data.

As shown in figure 2, during the 'necking between voids' phase there is interaction between the

voids. Due to these interactions the internal strength is decreased. In order to incorporate this phenomenon a modified volume fraction of voids f^* is introduced instead of original volume fraction of voids f. The main idea of this modified formulation is that after a certain value the volume fraction of voids changes. As mentioned in [23], f^* can be expressed as follows,

$$\begin{aligned} f^*(f) &= \begin{cases} f, & f \leq f_c \\ f_c + \kappa(f - f_c), & f > f_c \end{cases} \\ \kappa &= \frac{f_u^* - f_c}{f_f - f_c} \end{aligned} \tag{2.2}$$

where f_c is the critical volume fraction after which the voids start interacting. Therefore before this value there is no modification the volume fraction of voids, i.e. f^* is analogous to f. f_f is the volume fraction of voids at macroscopic failure. After the interaction of voids starts, $f^* = f^*(f_f)$. κ introduced in the formulation serves the purpose of an accelerating factor.

For the sake of calculation volume fraction of voids is prescribed for the material before the plastic flow. Due to local stress and strain these voids will grow and also new voids will be created. The void evolution law considers an initial volume fraction of voids f_0, describes the growth of voids based on the assumption of incompressibility of the material and the creation of new voids through $f_{nucleation}$. Strain controlled the $f_{nucleation}$. Therefore the evolution of volume fraction of voids can be written as

$$\dot{f} = \dot{f}_{growth} + \dot{f}_{nucleation}. \tag{2.3}$$

Void growth is ruled by the incompressibility of materials surrounding the voids. Thefore, considering the mass balance following can be written.

$$\dot{f}_{growth} = (1 - f)\dot{\varepsilon}_{kk}^{pl} \tag{2.4}$$

where $\dot{\varepsilon}_{kk}^{pl}$ is the volume dilation rate. For the nucleation of voids a statistic Gaussian distribution is assumed.These new voids have a volume fraction of f_N as per assumption. These arise at the mean equivalent strain of ε_N with a specific standard deviation S_N. Therefore as per [23], it can be written that

$$\begin{aligned} \dot{f}_{nucleation} &= A.\dot{\bar{\varepsilon}}^{pl}, \\ A &= \frac{f_N}{S_N.\sqrt{2\pi}}.\exp\left[-\frac{1}{2}\left(\frac{\bar{\varepsilon}^{pl} - \varepsilon_N}{S_N}\right)^2\right]. \end{aligned} \tag{2.5}$$

Here $\bar{\varepsilon}^{pl}$ is the equivalent plastic strain. Void nucleation is proportional to the equivalent plastic strain and total available nucleation density f_N. Finally when the volume fraction of voids reach the value of f_f, the voids coalescence and a meso-crack initiates. In GTN model, localization of plastic strain is coupled with the final failure.

3 Method Implementation

In this chapter a data analysis methodology is proposed to optimize the unknown parameters of GTN model.

3.1 Internal parameters

Although GTN model is very useful to describe the ductile fracture, it has a certain disadvantages as already pointed out in section 2.2. It has 12 unknown parameters in the mathematical formulation, which needs to be determined. Some of those can be determined by experimental methods but most of them has to be found out through an iterative method. In this work 11 parameters are considered as unknown and the parameter matrix $\mathbf{P}$, containing these 12 parameters can be represented as

$$\mathbf{P} = p_i = (\sigma_0 \quad \varepsilon_0 \quad q_1 \quad q_2 \quad q_3 \quad f_0 \quad f_c \quad f_f \quad f_N \quad \varepsilon_N \quad S_N)^T. \tag{3.1}$$

Referring to equation 3.1, σ_0 and ε_0 can be filtered out as the parameters which can be measured directly from the experiments. f_0 or the initial volume fraction of the voids can be measured from the relative density. The standard deviation S_N has a very little influence on the outcome of model. As per Abaqus manual section 1.1.9 the value of S_N can be taken as 0.05. q_1 and q_2 have similar kind of influence on the model outcome and therefore it is sufficient to vary only one of them. As per the Abaqus documentation, q_3 can be expressed as square of q_1, i.e. $q_3 = {q_1}^2$. Therefore, in this work only q_1 is chosen as unknown in this work. The value of q_2 is taken as 1.0 referring to the Abaqus documentation. Finally, as a summary of the above paragraph it can be concluded that the Parameter matrix further reduces to $\mathbf{P}_{\text{Opt}}$. This contains only the parameters to be optimized.

$$\mathbf{P}_{\text{Opt}} = (\quad q_1 \quad f_c \quad f_f \quad f_N \quad \varepsilon_N)^T. \tag{3.2}$$

3.2 Parameter optimization through data optimization method

For determination of the internal parameters a lot of methods are prescribed in literature. See [20], [24] and [25], where different optimization algorithm is adopted to predict these internal parameters of GTN model. In this work, the response surface method is implemented to predict these internal parameters.

Within the response surface method, machine learning is used as a tool. The machine learning is a very popular tool in recent years for optimization. It has a lot of other scopes as well. Machine learning is the process of decision making by machines through analysis of past data.

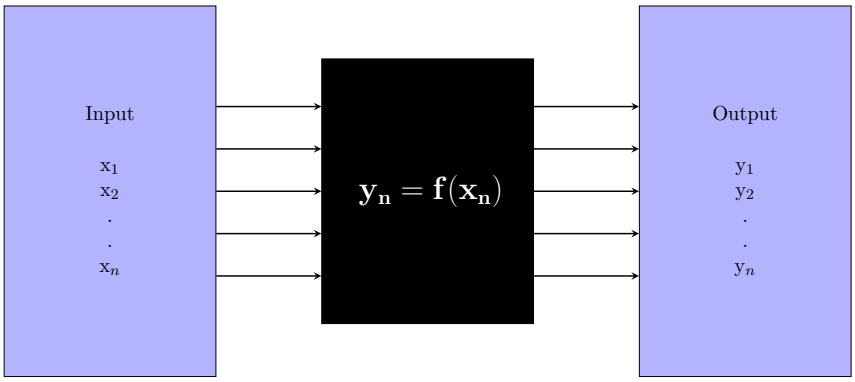

Figure 3 Block diagram of a simple machine learning problem, where the input and output data is known and function relating the input and output, data is unknown. this unknown function is shown inside the black box

A simple example of a machine learning problem is shown in figure 3. In every problem we will have a set of input data (x_1, x_2, ..., x_n) and a set of output data (y_1, y_2, ..., y_n) as can be seen in figure 3. These data can be a scalar or a vector. These provided data are called the training set of data. Using statistical methods, the machine learning algorithm predicts the function that converts the input data into output data. As per figure 3, f(x_n) shown in the black box is the function to be predicted through the machine learning algorithm.

Machine learning problems can be broadly classified into two types. They are :

1. **Classification problem:** This kind of problem deals with the situations where we have to classify between two or more objects. For an example, recognition of alphabets in the handwritten note is a classification problem. In this particular case, the training set of data can be the geometry of the alphabets in a known font (e.g. times new roman). An example of a handwritten note is shown in figure 4.

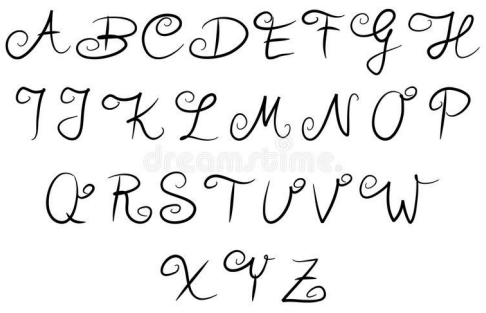

Figure 4 Example of classification problem: classifying the handwritten alphabets, see [26] for reference

2. **Regression problem:** This kind of problem deals with a situation where we need to interpolate the data from present and past in the future from the available data. For an example, the prediction of path of a robot arm from the movement of joints is a regression problem. In this case, the training data set could be the joint position and arm position from the past experience.

In this work, the input data are the stress-load curve. So each input is a vector and the output parameter is the parameters of $\mathbf{P}_{\text{Opt}}$. A machine learning algorithm is proposed to predict the input parameter from any stress-strain curve. This problem can be categorized as a regression problem.

3.3 Data Generation

In this work, a rod of diameter 1.25 mm and length 20 mm is created using Abaqus. However, the simulation model size is different compared to the experimental specimen. This work is only trying to proof the feasibility of the proposed method. Material is selected as 316L steel with GTN model implemented as its failure model. The values of Parameters from $\mathbf{P}_{\text{Opt}}$ is chosen from table 1.

Parameter	Lower limit	Upper limit	Set of values
q_1	1.0	1.6	[1.0, 1.2, 1.4, 1.6]
ε_N	0.1	0.4	[0.1, 0.2, 0.3, 0.4]
f_N	0.01	0.04	[0.01, 0.02, 0.03, 0.04]
f_C	0.1	0.16	[0.1, 0.12, 0.14, 0.16]
f_F	0.2	0.5	[0.2 0.3 0.4 0.5]

Table 1 Range of parameters of $\mathbf{P}_{\text{Opt}}$ taken for simulation

It can be calculated that a total of 1024 combinations of values can be taken as an input from table 1. However due to numerical problems, some of the simulation results are deleted and finally 960 simulation results are taken into account. Among these simulation results, 80% results are randomly chosen as training data set. These data are used to establish a relation between the input data, i.e. stress values at reference points and the the desired output, i.e. the parameters. After finding the relation, it is applied to the stress result of test data set and the obtained value of parameters of $\mathbf{P}_{\text{Opt}}$ are then compared with the values obtained from the Abaqus simulation result to check the validity of the established relation. This process is explained in detail in section 3.4 and section 3.5.

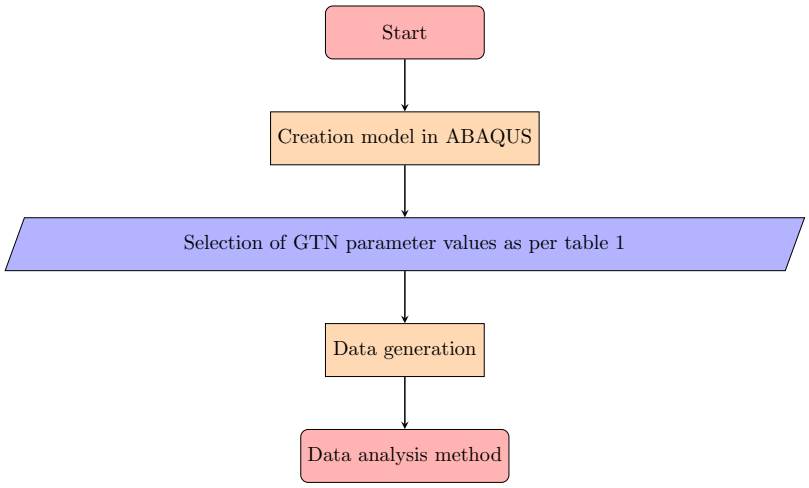

Figure 5 Block diagram for data generation process

3.4 Data analysis method

As mentioned in section 3.2, Response surface methodology (RSM) is used as a tool for analysis of data in this work. RSM was first introduced by George E. P. Box and K. B. Wilson in 1951. This is recognized as a statistical method that explores for a relationship between explanatory variables and one or more response variables. Within RSM, a sequence of designed experiments are performed to obtain an optimal relationship. Box and Wilson proposed a second-degree polynomial for approximation. In this work, a machine learning algorithm is used as an approximation method. In our case, the stress values at fixed reference point are explanatory variables and the GTN model parameters are response variable.

Therefore, the machine learning algorithm within the RSM takes the stress-strain curve as input and the values of parameters of $\mathbf{P}_{\text{Opt}}$ as output data. The algorithm works in two main steps for prediction of the relation between the input and output. In the first step, it predicts the relation between the stress-strain and first three parameters from $\mathbf{P}_{\text{Opt}}$, i.e. q_1, ϵ_N and f_N. In the second step, the training data is divided into categories based on the value of q_1. We have four possible values of q_1 in this work as per table 1. Therefore, we will have four categories of training data. Finally a relation is established between the stress-strain curve and last two parameters of $\mathbf{P}_{\text{Opt}}$, i.e. f_c and f_f for each category. Figure 6 shows a rough flow of operations explained above.

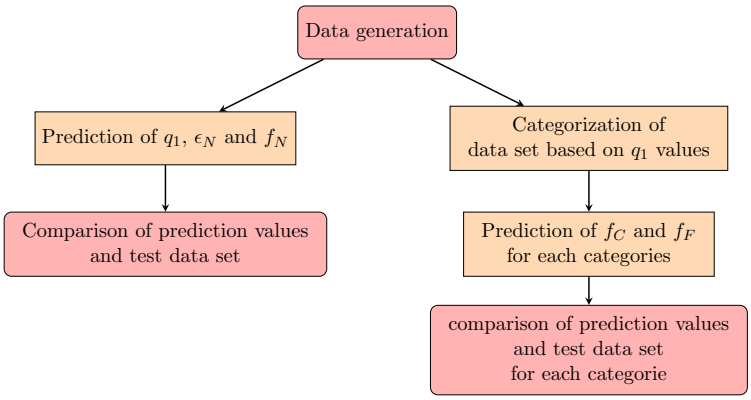

Figure 6 Basic structure of the proposed machine learning algorithm

Prediction of q_1, ϵ_N and f_N: In this step the input is that part of the stress-strain curve, which is responsible for void nucleation. In this work, only four points are chosen from the stress-strain curve. These points range from 8th to 11th point of the curve. Therefore according to figure 3, it can be said that the input in this case is a vector containing four points, which can be expressed as following:

$$\mathsf{x}_n = \begin{pmatrix} S_8 \\ S_9 \\ S_{10} \\ S_{11} \end{pmatrix} = \begin{pmatrix} \mathsf{x}_{n1} \\ \mathsf{x}_{n2} \\ \mathsf{x}_{n3} \\ \mathsf{x}_{n4} \end{pmatrix}. \tag{3.3}$$

Where S_8, S_9, S_{10} and S_{11} are the 8th , 9th, 10th, 11th points of the stress-strain curve. The outputs y_n shown in figure 3 are taken as a functions of q_1, ϵ_N and f_N. In this work three functions are chosen, as shown in equation 3.4.

$$\begin{aligned} Y_1 &= q_1 + 2\epsilon_N + 20 f_N, \\ Y_2 &= q_1 + 4\epsilon_N + 20 f_N, \\ Y_3 &= q_1 + 2\epsilon_N + 40 f_N. \end{aligned} \tag{3.4}$$

From these functions Y_n, the parameters q_1, ϵ_N and f_N can be retrieved using the following formulas.

$$\begin{aligned} q_1 &= 3Y_1 - Y_2 - Y_3 \\ \epsilon_N &= \frac{(Y_2 - Y_1)}{2} \\ f_N &= \frac{(Y_3 - Y_1)}{20} \end{aligned} \tag{3.5}$$

Thereafter, the following function is proposed for relating the Y_n and x_n.

$$Y_n = \sum_{i=1}^{4} C_i X_{ni} + \sum_{i=1}^{4} C_{(i+4)} X_{ni}^2 + \sum_{i=1}^{4}\sum_{j=1}^{4} C_{(4i+j+3)} X_{ni} X_{nj} \tag{3.6}$$

Using MATLAB, the coefficients C_n (n=1, 2, ..., 14) is found out. Training data set is used as a reference. Thereafter, putting the value of these coefficients the relation Y_n=$f_1(x_n)$ is established. This function is then applied to the whole data set to find the predicted Y_n, which can referred to as $Y_{n_{Pr}}$ (n= 1, 2, 3). From the values of $Y_{n_{Pr}}$, the predicted values of q_1, ϵ_N and f_N are calculated using 3.5, which can be referred to as $q_{1_{Pr}}$, $\epsilon_{N_{Pr}}$ and $f_{N_{Pr}}$. This predicted data is then compared with the original data and the relative error is calculated, which can be expressed by means of the following equation.

$$\text{Relative Error of } \{q_1,\ \epsilon_N,\ f_N\} = \frac{\{q_1,\ \epsilon_N,\ f_N\}_{Pr} - \{q_1,\ \epsilon_N,\ f_N\}}{\{q_1,\ \epsilon_N,\ f_N\}} \tag{3.7}$$

Finally the cumulative probability of having a prediction with a permissible error is calculated for the training and test data. In this work, the permissible relative error is taken as 0.25. For each parameter this probability is calculated separately. This is done using the following formula.

$$\text{Cumulative probability of data set} = \frac{\text{Number of data set with relative error} \leq Permissibleerror}{\text{Number of elements in data set}} \tag{3.8}$$

From these probabilities, it can be understood that how effective the machine learning algorithm is in predicting the parameters (q_1, ϵ_N and f_N) from a stress-strain curve.

Prediction of f_C and f_F: During prediction of f_C and f_F, the data set is categorized according to the value of q_1. Since in this work all the data is taken from the table 1, 4 categories are created. This categorization is done separately for training and test data set. For each category prediction algorithm is run separately. Since f_C and f_F are the related to the failure of the material, therefore as an input parameter a part of stress-strain curve is chosen, which is responsible for failure of the material. In this work, three points from the curve are chosen for this step. These points are in the range of 15th to 17th in the stress-strain curve. As before, the input data can be expressed as following.

$$x_n = \begin{pmatrix} S_{15} \\ S_{16} \\ S_{17} \end{pmatrix} = \begin{pmatrix} x_{n1} \\ x_{n2} \\ x_{n3} \end{pmatrix}, \tag{3.9}$$

where S_{15}, S_{16} and S_{17} are the 15th, 16th and 17th points respectively in the stress-strain curve. The output in this case are functions of f_C and f_F. These functions can be expressed

as following.

$$\begin{aligned} Y_1 &= f_C + 3f_F, \\ Y_2 &= f_C + 6f_F. \end{aligned} \tag{3.10}$$

From these functions f_C and f_F can be retrieved using the following formulas.

$$\begin{aligned} f_C &= 2Y_1 - Y_2, \\ f_F &= \frac{Y_1 - Y_2}{3}. \end{aligned} \tag{3.11}$$

The proposed function, relating Y_n and x_n for the case of prediction of f_C and f_F is as follows.

$$Y_n = \sum_{i=1}^{3} C_i X_{ni} + \sum_{i=1}^{3} C_{(i+4)} X_{ni}^2 + \sum_{i=1}^{3}\sum_{j=1}^{4} C_{(3i+j+2)} X_{ni} X_{nj} \tag{3.12}$$

As in the case of prediction of q_1, ϵ and f_N, in this case also the coefficients C_n (n= 1, 2, 3, ..., 9) are found taking the training data as a reference using MATLAB. Thereafter, using this values in equation 3.12 the function relating Y_n and x_n can be determined. Using that function the value of output Y_n is calculated and thereafter using equation 3.11, the values of f_C and f_F is predicted for training and test dataset. As comparison of original and predicted data, relative error is calculated and the cumulative probability of having a relative error less than or equal to 25% is calculated for each parameter for each category.

3.5 Statistical analysis for model validation and improvement

In this section, statistical tools are used to validate the above mentioned data analysis method. An effort to relate the results of two different steps of the above mentioned machine learning algorithm is also made in this section. Therefore, the set Ω = { f_C, f_F } is assumed the set of output parameters and the set Φ = {q_1, ϵ_N, f_N} is the set of input parameters. We calculate the probability of the parameters from Ω for given values of the parameters from Φ. In mathematical terms, this probability can be termed as posterior probability and can be represented as

$$P(\Omega|\Phi) = P(f_C \text{ or } f_F|q_1, \epsilon_N, f_N). \tag{3.13}$$

One example of the posterior probability can be $P(f_C = 0.1|q_1 = 1.0, \epsilon_N = 0.1, f_N = 0.01)$. Since during the data generation process, values are taken according to table 1. Therefore, it can be understood that there are 256 posterior probabilities for f_C for different combinations of f_C, q_1, ϵ_N and f_N. Same number of posterior probabilities are there for f_F. These probabilities are calculated from the generated data and from the predicted results separately. Finally a

relative error of posterior probability for the predicted value with respect to the generated data is calculated. All the dataset, for which the relative probability is less than 25% predicted values are reported. For all other cases, more additional data has to be created. As a continuation of this work 5024 data are created for further application of the same method on the data for which the relative error of posterior probability is greater than permissible error. In this work permissible error is taken as 0.25. An iterative process for finding the correct prediction with increased number of training data set will be part of further work. In this work, results for one iteration loop is shown. A brief description of the whole process is given in figure 7 in the form of a flow chart.

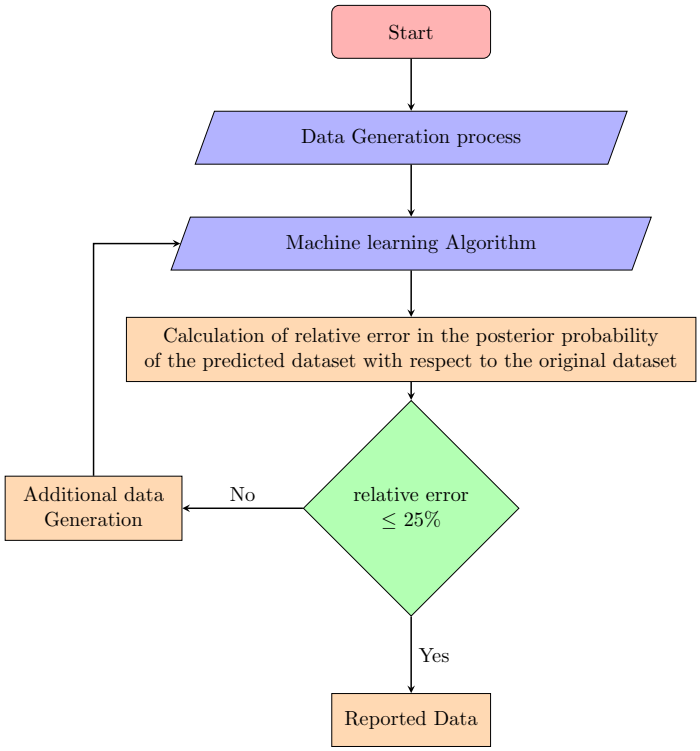

Figure 7 Flow chart for the whole Optimization process

4 Results

In this section, a data set of 960 data is generated in ABAQUS. The data analysis method is implemented on the generated dataset and cumulative probabilities for each parameter is calculated. Thereafter relative error of Posterior probability is calculated.

4.1 Data Generation

As mentioned in section 3.3, a model of Φ 1.25mm $\times$ 20mm rod is created in Abaqus, which shown in the figure 8 in its reference configuration, i.e. without any deformation. The material of this rod is 316L steel. GTN model is implemented as the failure model of the material. The parameters of $\mathbf{P}_{\text{Opt}}$ are chosen from table 1. This rod is subjected to the tensile test. In this

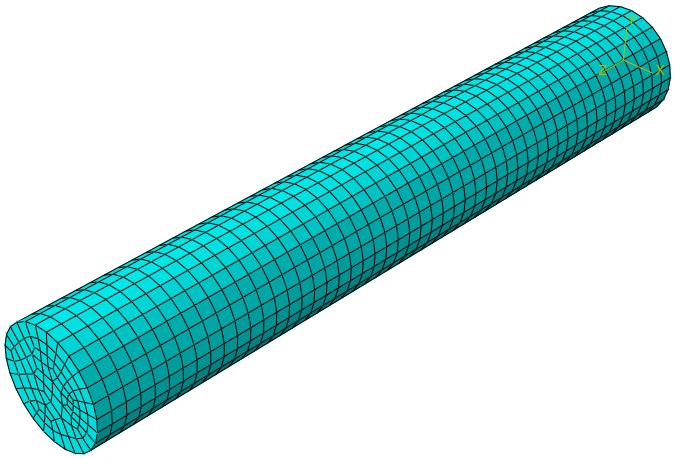

Figure 8 Model of rod in reference configuration in Abaqus

section the result are shown for only one combinations out of a total of 960 combination.
As the first combination of parameters q_1= 1.0, ϵ_N= 0.1, f_N= 0.01, f_C= 0.1 and f_f= 0.2 are chosen. In figure 9, the Von-Mises stress after the tensile test is shown. The stress varies from 4.775 $\times$ 10^{-4} to 1.076 $\times$ 10^{-3} MPa. In figure 9, the distribution of void volume fraction after the tensile test is shown. The void volume fraction varies from 1.016 $\times$ 10^{-3} to 1.701 $\times$ 10^{-2}. In figure 10, the distribution of growth of void volume fraction after the tensile test is shown. The value varies from 5.635 $\times$ 10^{-7} to 6.235 $\times$ 10^{-3}. In figure 10 the nucleation of void volume fraction after the tensile test is shown. The value varries from 1.635 $\times$ 10^{-5} to 9.772 $\times$ 10^{-3}. Figure 13 shows the evolution of Void volume fraction with respect to time.
960 times simulation is run and the data set is generated. In figure 14 the stress-strain curves for all 960 combinations are plotted. As mentioned in section 3.4, the zone marked by red rectangle shown in figure 14 are taken as the basis for predicting q_1, ϵ_N and f_N and the zone

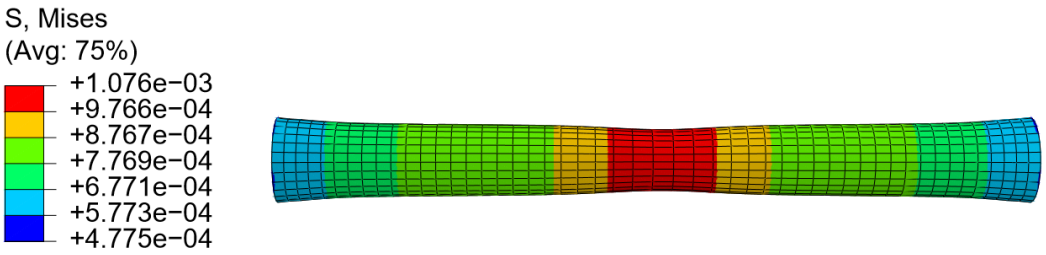

Figure 9 Distribution of stress in the deformed rod

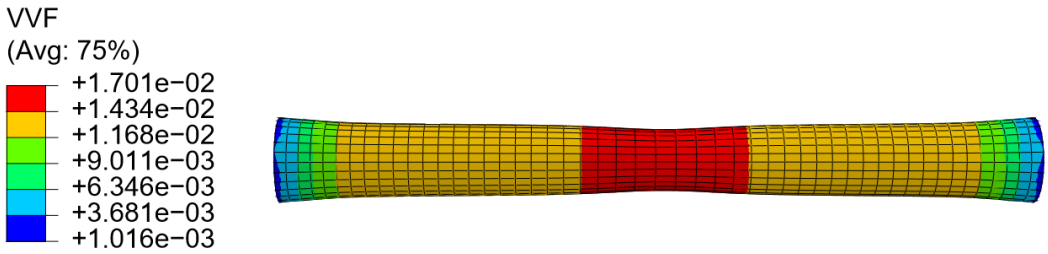

Figure 10 Distribution of Void volume fraction in the deformed rod

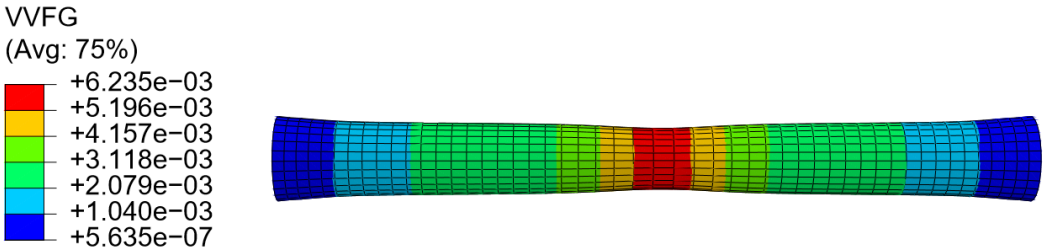

Figure 11 Distribution of growth of Void volume fraction in the deformed rod

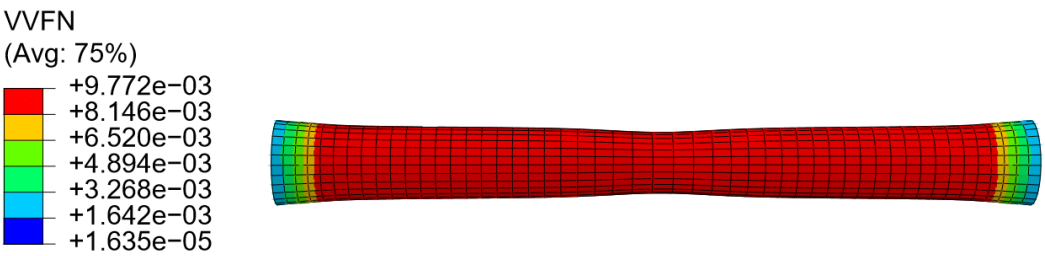

Figure 12 Distribution of growth of Void volume fraction in the deformed rod

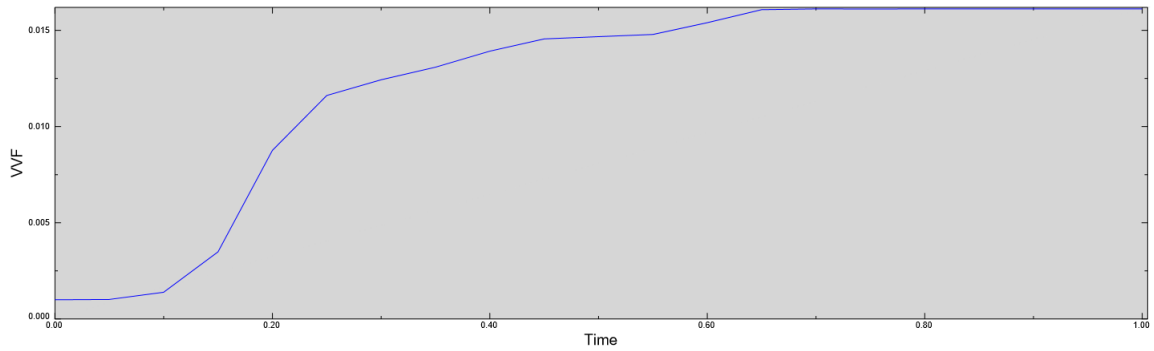

Figure 13 Evolution of void volume fraction with respect to time

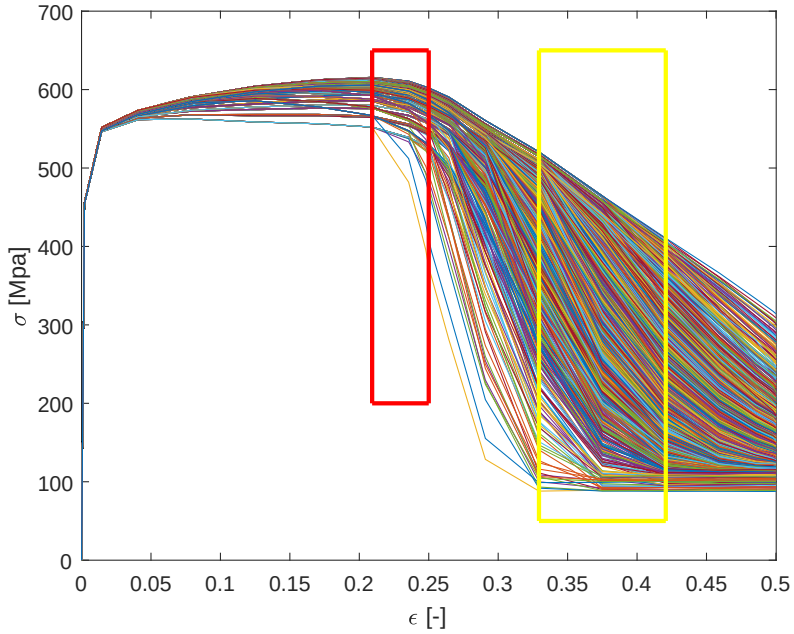

Figure 14 Stress-strain curve

marked by yellow rectangle shown in figure 14 are taken as the basis for predicting f_F and f_C.

4.2 Data Analysis Method

The Data Analysis method described in section 3.4 is implemented in the generated data. As a first step q_1, ϵ_N and f_N is predicted. The cumulative probability is calculated for the training data and test data separately as shown in equation 3.8. A variation of cumulative probability of correct prediction with respect to different permissible relative error is shown for training data and test data separately in figure 15 and 16 respectively. As can be seen in the figures, there is increase in the number of correctly predicted data if the permissible relative error is increased.

As a second step the prediction algorithm is run for prediction of f_C and f_F. In this step the data is divided in four categories according to the values of q_1. Referring table 1, we know that we only have 4 different values of q_1. Therefore we have four categories of data in this step.

Cumulative probability of correct prediction of f_C and f_F for different permissible relative error is plotted in figure 17 to figure 20 for four different categories. In this step also, we have a convergence of cumulative probability to 1 with the increase of permissible error. In this work, we take the permissible relative error as 0.25 for both steps.

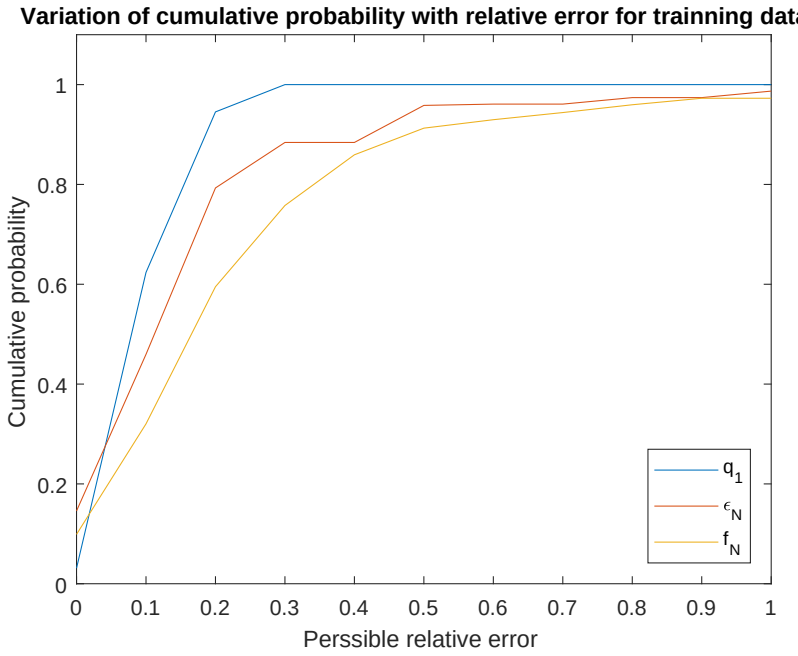

Figure 15 Cumulative probability of correct prediction of q_1, ϵ_N and f_N for training data with different permissible relative error of prediction

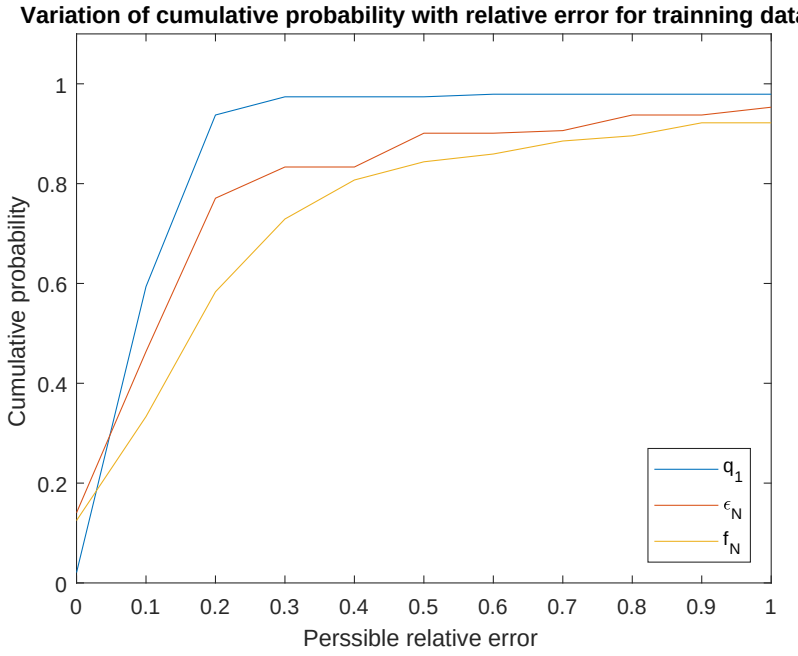

Figure 16 Cumulative probability of correct prediction of q_1, ϵ_N and f_N for training data with different permissible relative error of prediction

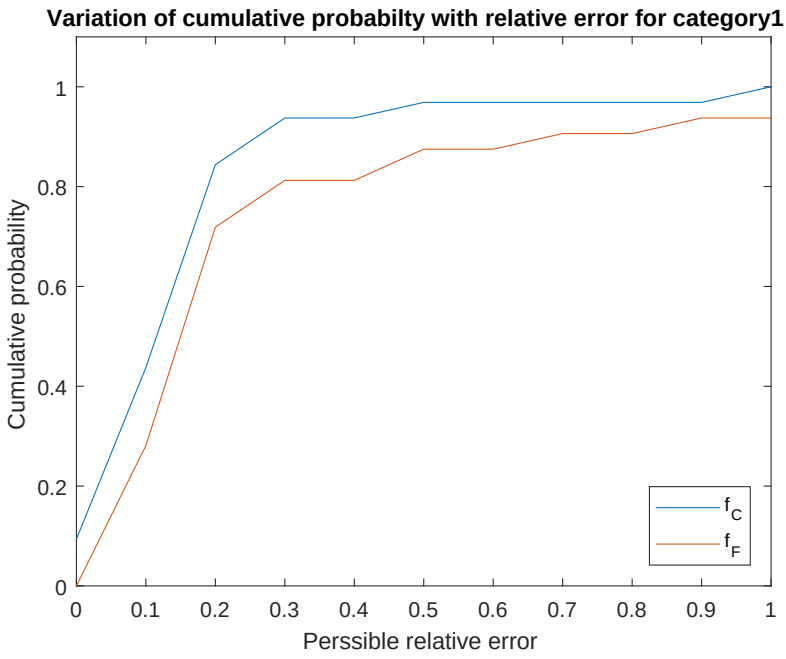

Figure 17 Cumulative probability of correct prediction of f_C and f_F for category 1 (i.e. q_1= 1.0) with different permissible relative error of prediction

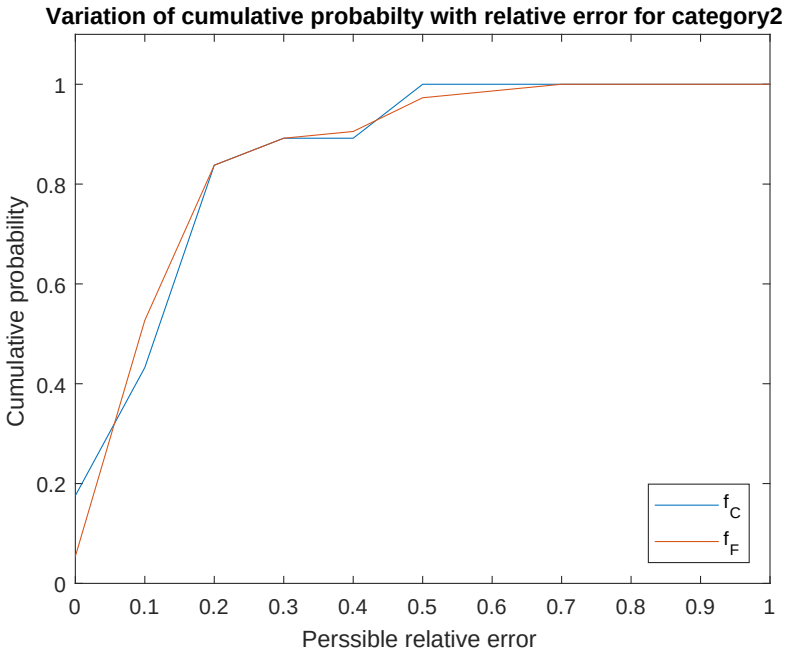

Figure 18 Cumulative probability of correct prediction of f_C and f_F for category 2 (i.e. q_1= 1.2) with different permissible relative error of prediction

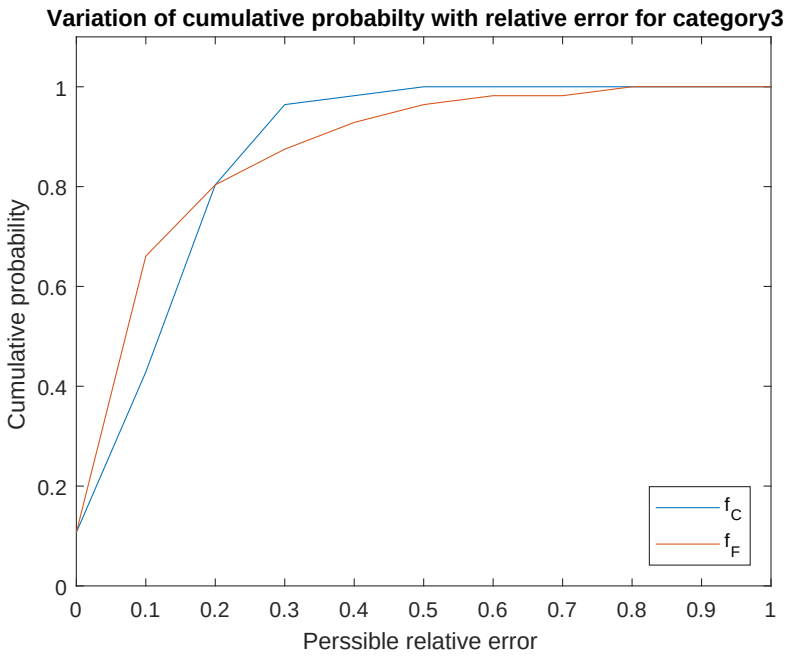

Figure 19 Cumulative probability of correct prediction of f_C and f_F for category 3 (i.e. q_1= 1.4) with different permissible relative error of prediction

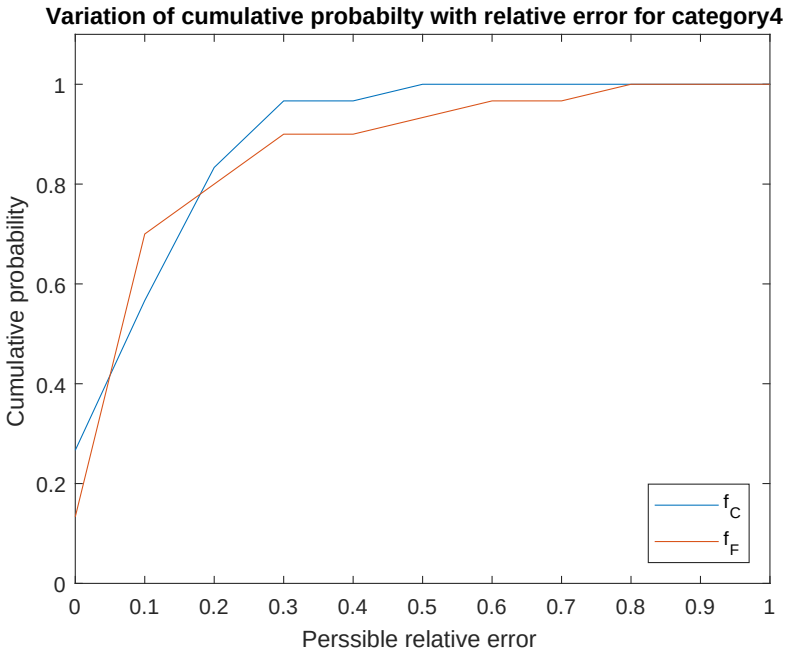

Figure 20 Cumulative probability of correct prediction of f_C and f_F for category 4 (i.e. q_1= 1.6) with different permissible relative error of prediction

4.3 Model validation results

In this section, a relation of two steps of data analysis method is established through implementation of statistical tool. Firstly, for different categories (i.e. for different values of q_1) and different values of ϵ_N and f_N probability of having a specific value of f_C or f_F is calculated. In section 3.5, this term is already mentioned as posterior probability. The posterior probability is calculated for the generated 960 data and the for the predicted test data. Thereafter, the relative error of these two values are calculated. From figure 21 to figure 24 show the relative error of posterior probability for f_C and from figure 25 to figure 28 show the relative error in posterior probability for f_F. These results are shown for the first loop of iteration, as mentioned in section 3.5. Thereafter the first loop of iteration is run for 50 times by randomly choosing 80% of data out of 960 data as the training set of data.

$$\begin{aligned}\text{Relative error of posterior probability for } f_C &= \frac{P(f_C|q_1,\epsilon_N,f_N)_{\text{960 data}} - P(f_C|q_1,\epsilon_N,f_N)_{\text{predicted data}}}{P(f_C|q_1,\epsilon_N,f_N)_{\text{960 data}}}\\ \text{Relative error of posterior probability for } f_F &= \frac{P(f_F|q_1,\epsilon_N,f_N)_{\text{960 data}} - P(f_F|q_1,\epsilon_N,f_N)_{\text{predicted data}}}{P(f_F|q_1,\epsilon_N,f_N)_{\text{960 data}}}\end{aligned} \tag{4.1}$$

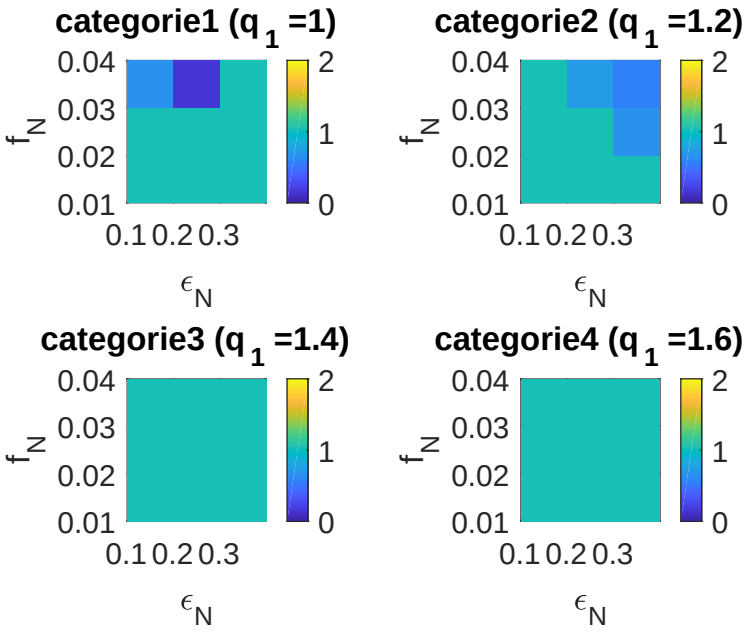

Figure 21 Variation of relative error of posterior probability of f_C=0.1 over the whole region on ϵ_N and f_N for different categories

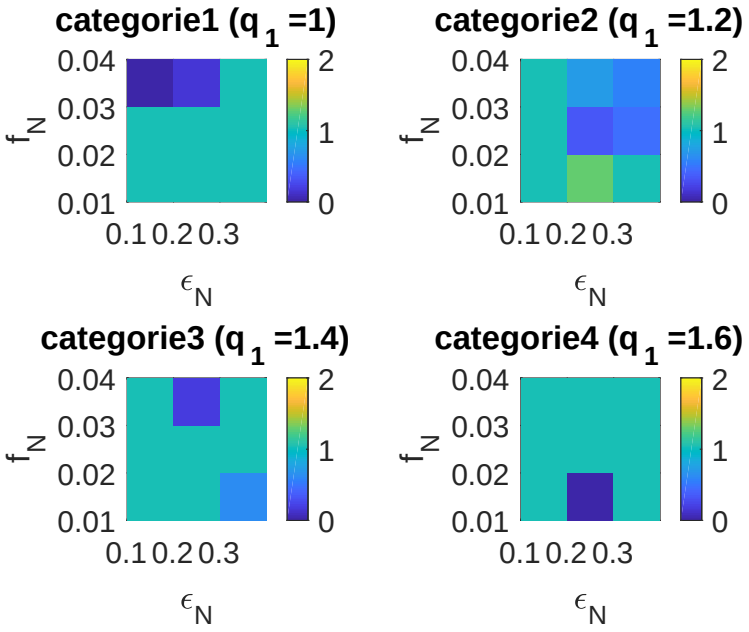

Figure 22 Variation of relative error of posterior probability of f_C=0.12 over the whole region on ϵ_N and f_N for different categories

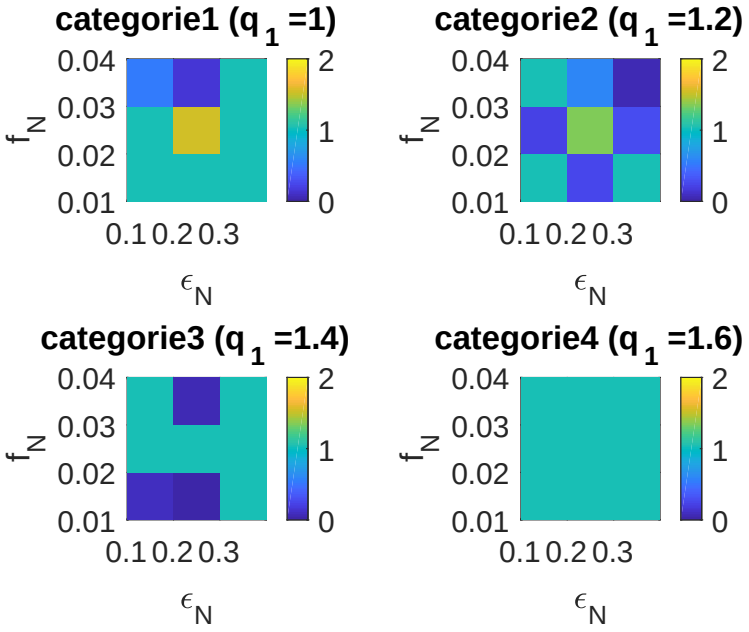

Figure 23 Variation of relative error of posterior probability of f_C=0.14 over the whole region on ϵ_N and f_N for different categories

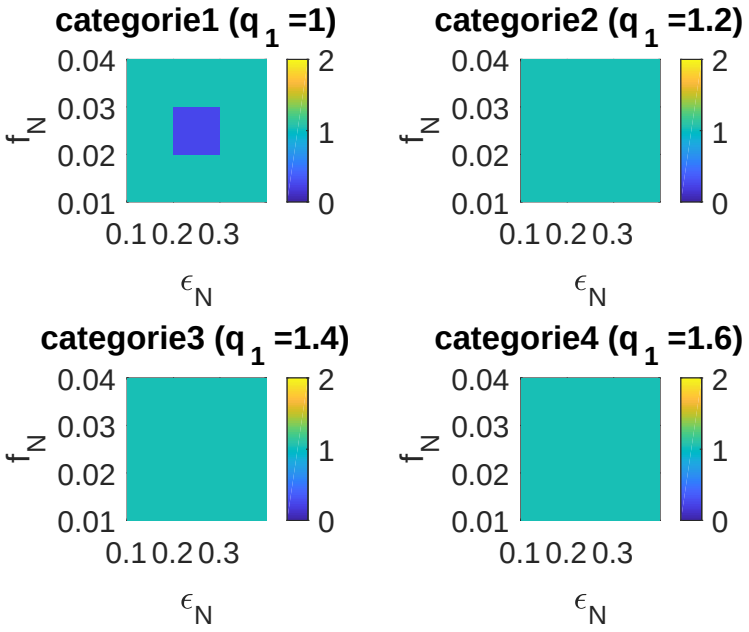

Figure 24 Variation of relative error of posterior probability of f_C=0.16 over the whole region on ϵ_N and f_N for different categories

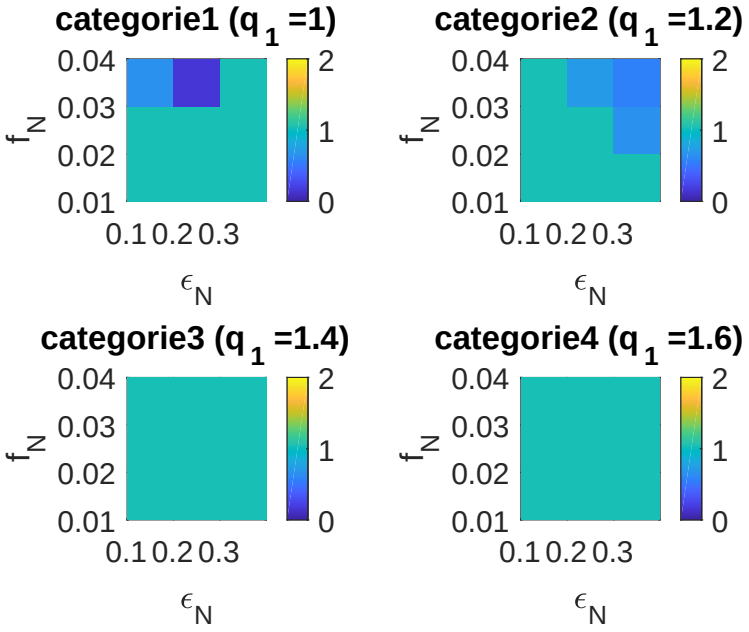

Figure 25 Variation of relative error of posterior probability of f_F=0.2 over the whole region on ϵ_N and f_N for different categories

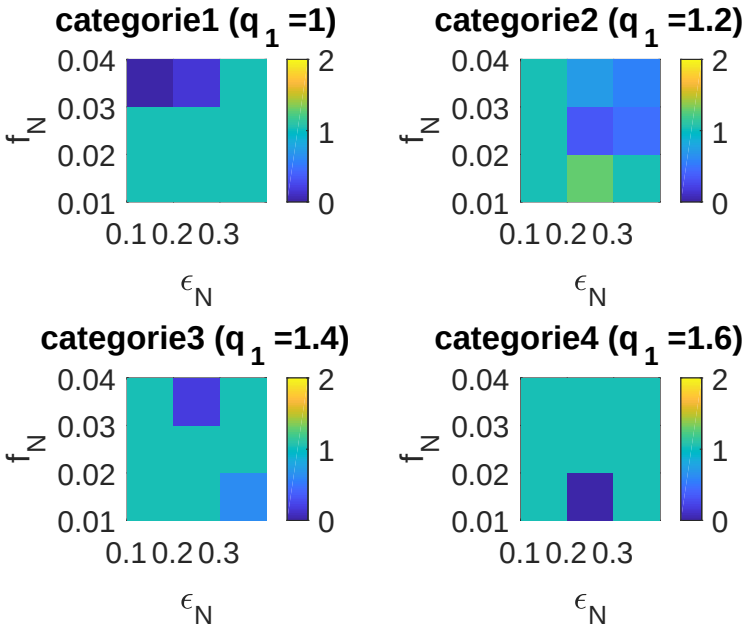

Figure 26 Variation of relative error of posterior probability of f_F=0.3 over the whole region on ϵ_N and f_N for different categories

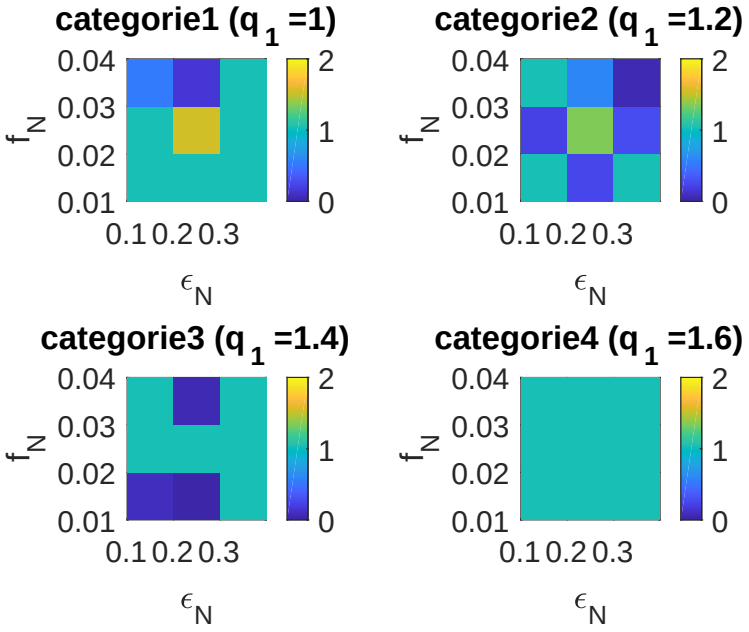

Figure 27 Variation of relative error of posterior probability of f_F=0.4 over the whole region on ϵ_N and f_N for different categories

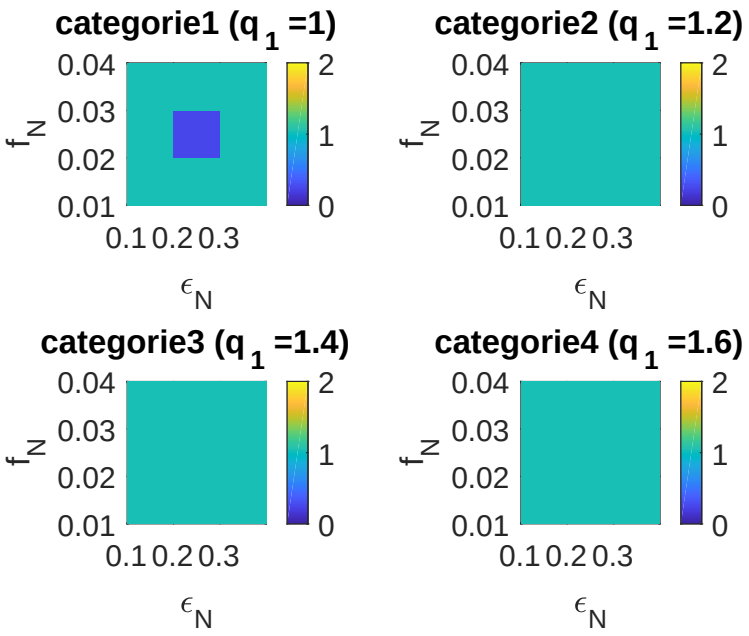

Figure 28 Variation of relative error of posterior probability of f_F=0.5 over the whole region on ϵ_N and f_N for different categories

Figure 29 and 30 shows the number of data fitting the condition of a relative error of posterior probability to be less than 0.25. This can also be interpreted as the number of correctly predicted data for the first loop of iteration

4.4 Further work

In order to get a better percentage of correctly predicted data, the present algorithm can be extended with a iteration loop as suggested in figure 7. In the next iteration step, the algorithm has to generate more data for the wrongly predicted data from the previous step of iteration.

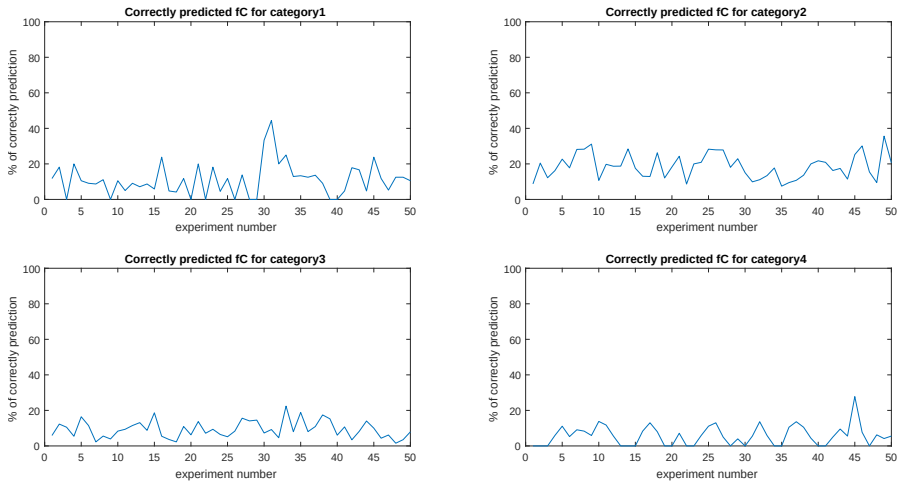

Figure 29 Percentage of correctly predicted data in terms of f_C for different experiments

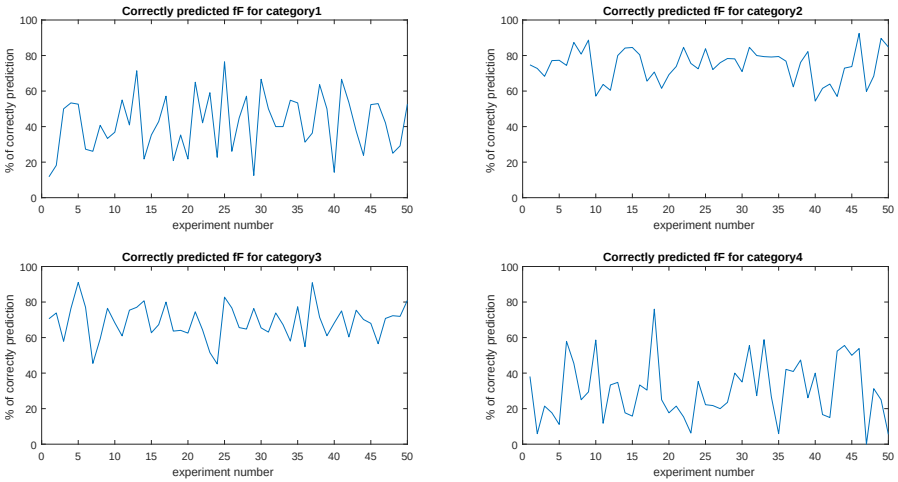

Figure 30 Percentage of correctly predicted data in terms of f_F for different experiments

In the next step of iteration, the same algorithm can be run and the predicted data can be validated using posterior probability. During the present work, 5024 data are created for the next iteration step as a first step of this further work.

5 Bibliography

[1] M. Averyanova, E. Cicala, P. Bertr, and D. Grevey, “Experimental design approach to optimize selective laser melting of martensitic 17-4 ph powder: part i–single laser tracks and first layer,” *Rapid Prototyping Journal*, vol. 18, no. 1, pp. 28–37, 2012.

[2] A. B. Spierings and G. Levy, “Comparison of density of stainless steel 316l parts produced with selective laser melting using different powder grades,” in *Proceedings of the Annual International Solid Freeform Fabrication Symposium*, pp. 342–353, Austin, TX, 2009.

[3] E. Yasa and J.-P. Kruth, “Microstructural investigation of selective laser melting 316l stainless steel parts exposed to laser re-melting,” *Procedia Engineering*, vol. 19, pp. 389–395, 2011.

[4] S. Leuders, M. Thöne, A. Riemer, T. Niendorf, T. Tröster, H. Richard, and H. Maier, “On the mechanical behaviour of titanium alloy tial6v4 manufactured by selective laser melting: Fatigue resistance and crack growth performance,” *International Journal of Fatigue*, vol. 48, pp. 300–307, 2013.

[5] B. Van Hooreweder, D. Moens, R. Boonen, J.-P. Kruth, and P. Sas, “Analysis of fracture toughness and crack propagation of ti6al4v produced by selective laser melting,” *Advanced Engineering Materials*, vol. 14, no. 1-2, pp. 92–97, 2012.

[6] W. E. Frazier, “Metal additive manufacturing: a review,” *Journal of Materials Engineering and Performance*, vol. 23, no. 6, pp. 1917–1928, 2014.

[7] T. Caffrey, “Additive manufacturing and 3d printing state of the industry annual worldwide progress report,” *Engineering Management Research*, vol. 2, no. 1, pp. 209–222, 2013.

[8] M. Foust, D. Thomsen, R. Stickles, C. Cooper, and W. Dodds, “Development of the ge aviation low emissions taps combustor for next generation aircraft engines,” in *50th AIAA Aerospace Sciences Meeting including the New Horizons Forum and Aerospace Exposition*, p. 936, 2012.

[9] C. Holshouser, C. Newell, S. Palas, L. J. Love, V. Kunc, R. F. Lind, P. D. Lloyd, J. C. Rowe, C. A. Blue, C. E. Duty, W. H. Peter, and R. R. Dehoff, “Out of bounds additive manufacturing,” *Advanced Materials and Processes*, vol. 171, no. 3, 2013.

[10] J. Sundseth and J. Berg-Johnsen, “Prefabricated patient-matched cranial implants for reconstruction of large skull defects,” *Journal of central nervous system disease*, vol. 5, pp. JCNSD–S11106, 2013.

[11] L. Mullen, R. C. Stamp, W. K. Brooks, E. Jones, and C. J. Sutcliffe, “Selective laser melting: A regular unit cell approach for the manufacture of porous, titanium, bone in-growth constructs, suitable for orthopedic applications,” *Journal of Biomedical Materials Research Part B: Applied Biomaterials*, vol. 89, no. 2, pp. 325–334, 2009.

[12] D. Leordean, C. Dudescu, T. Marcu, P. Berce, and N. Balc, "Customized implants with specific properties, made by selective laser melting," *Rapid Prototyping Journal*, vol. 21, no. 1, pp. 98–104, 2015.

[13] I. J. Petrick and T. W. Simpson, "3d printing disrupts manufacturing: how economies of one create new rules of competition," *Research-Technology Management*, vol. 56, no. 6, pp. 12–16, 2013.

[14] C. Thomas, W. Christopher, I. Olga, and G. Banning, "Could 3d printing change the world," *Technologies, Potential, and Implications of Additive Manufacturing, Atlantic Council, Washington, DC*, 2011.

[15] B. Berman, "3-d printing: The new industrial revolution," *Business horizons*, vol. 55, no. 2, pp. 155–162, 2012.

[16] Wikipedia, "Selective laser melting," 2018.

[17] G. Tapia, A. Elwany, and H. Sang, "Prediction of porosity in metal-based additive manufacturing using spatial gaussian process models," *Additive Manufacturing*, vol. 12, pp. 282–290, 2016.

[18] A. L. Gurson, "Continuum theory of ductile rupture by void nucleation and growth: Part i—yield criteria and flow rules for porous ductile media," *Journal of engineering materials and technology*, vol. 99, no. 1, pp. 2–15, 1977.

[19] V. Tvergaard and A. Needleman, "Analysis of the cup-cone fracture in a round tensile bar," *Acta metallurgica*, vol. 32, no. 1, pp. 157–169, 1984.

[20] M. Springmann and M. Kuna, "Identification of material parameters of the gurson–tvergaard–needleman model by combined experimental and numerical techniques," *Computational Materials Science*, vol. 33, no. 4, pp. 501–509, 2005.

[21] S. Gatea, H. Ou, B. Lu, and G. McCartney, "Modelling of ductile fracture in single point incremental forming using a modified gtn model," *Engineering Fracture Mechanics*, vol. 186, pp. 59–79, 2017.

[22] V. Tvergaard, "Influence of voids on shear band instabilities under plane strain conditions," *International Journal of fracture*, vol. 17, no. 4, pp. 389–407, 1981.

[23] W. Bleck, W. Dahl, A. Nonn, L. Amlung, M. Feldmann, D. Schäfer, and B. Eichler, "Numerical and experimental analyses of damage behaviour of steel moment connection," *Engineering Fracture Mechanics*, vol. 76, no. 10, pp. 1531–1547, 2009.

[24] M. Abbasi, B. Bagheri, M. Ketabchi, and D. Haghshenas, "Application of response surface methodology to drive gtn model parameters and determine the fld of tailor welded blank," *Computational Materials Science*, vol. 53, no. 1, pp. 368–376, 2012.

[25] M. Abendroth and M. Kuna, "Determination of deformation and failure properties of ductile materials by means of the small punch test and neural networks," *Computational Materials*

Science, vol. 28, no. 3-4, pp. 633–644, 2003.

[26] Dreamstime.com, “Casual handwritten alphabet, letters a-z in brush script style,” 2018.